Article:
Murasovs, N., Francescon, V., Lloyd, P. et al. (6 more authors) (2024) Breathing Compensation in Magnetic Robotic Bronchoscopy via Shape Forming. IEEE Robotics and Automation Letters, 9 (10). pp. 9055-9062. ISSN 2377-3766

https://doi.org/10.1109/lra.2024.3426385

Breathing Compensation in Magnetic Robotic Bronchoscopy via Shape Forming

Nikita Murasovs[1], Vittorio Francescon[1], Peter Lloyd[1], Michele Di Lecce[1], Damith S. Chathuranga[2], Giovanni Pittiglio[3], Onaizah Onaizah[4], James H. Chandler[1], and Pietro Valdastri[1]

***Abstract*—Despite the increased interest in robotic systems designed for bronchoscopy, the influence of the bronchial tree dynamics remains relatively unexplored. To enable robotic solutions to perform successful autonomous navigations whilst minimizing contact with the internal anatomy, they must be capable of adapting to ongoing geometric changes caused by the respiratory cycle. In this paper, we introduce a method for parameterizing these cyclic changes and present a flexible magnetic robotic catheter design that adapts its shape dynamically. Three bronchial branches (up to 4th generation bronchioles) with diverse shapes were investigated to examine the feasibility and efficacy of this approach. Reference anatomical geometry was taken from an open-source dynamic computed tomography patient dataset, and was evaluated over the breathing cycle to develop patient- and branch-specific magnetic catheter profiles and associated time-varying external magnetic fields. The system was demonstrated using dynamic Helmholtz coil actuation and showed a mean error in replicating the centerline of each of the three branches over the entire navigation of 2.1 mm, 1.4 mm, and 1.9 mm respectively.**

***Index Terms*—Medical Robots and Systems, Surgical Robotics: Steerable Catheters/Needles**

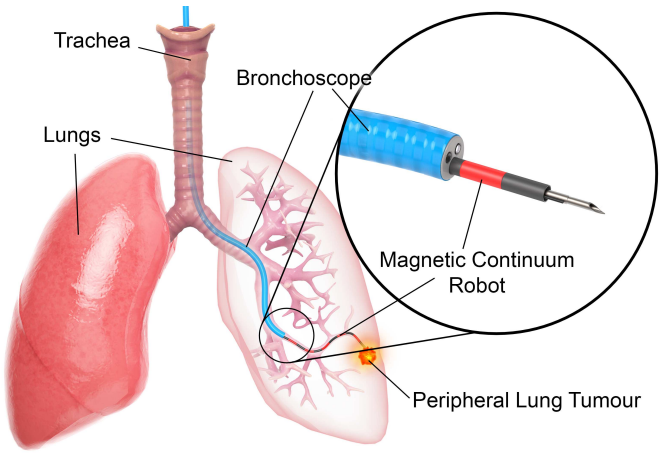

Fig. 1. Illustration of robotic bronchoscopy. Commercial bronchoscope shown in blue with a deployable MCR shown in a black-and-red pattern. The figure shows the overview of the autonomous navigation, where after initial navigation performed by the bronchoscope, MCR is deployed to steer through the deeper parts of the bronchial tree and deliver a tool (e.g. needle or laser) to the target tumour.

I. Introduction

LUNG cancer is responsible for the highest number of deaths of any cancer worldwide [1]. In bronchoscopy, a slender, flexible manipulator is inserted to visually inspect and facilitate the deployment of a catheter for the collection of tissue; which is the main method of confirming malignant lesions in the lungs. Transthoracic biopsies and surgical resection increase diagnostic yield but can result in complications such as pneumothorax and surgical morbidities [1]. Unlike conventional bronchoscopy, where diagnostic yield is less than 50% [1], robotic bronchoscopy can increase yield to as much as 90% [2] by improving instrument stabilization at biopsy and easing navigational challenges.

Commercial robotic bronchoscopy platforms such as Ion™ by Intuitive Surgical, Monarch™ by Auris Health, and Galaxy System™ by Noah Medical blue utilize a robotic bronchoscope (down to 3.5 mm in diameter) to navigate the upper parts of the bronchial tree while deploying manual pre-bent catheters to facilitate deeper access. These tools offer limited dexterity and rely on high stiffness for manual navigation, which can sometimes result in discomfort and injury [3]. To address this issue researchers are exploring the use of soft robotic manipulators as an alternative to commercial tools [4, 5]. Soft continuum robots are known for their high dexterity and multiple degrees of freedom, making them safer but more challenging to control as compared to rigid surgical tools [6]. Increasing the dexterity or shape-forming capacity of continuum robots typically leads to a larger diameter but, due to external actuation, this is not the case for magnetic continuum robots (MCRs) making them ideal for miniaturization [7, 8]. Various MCR designs have been proposed, including those with multiple embedded permanent magnets along their body [9, 10, 11] and those integrating magnetically doped elastomers [12, 13]. The former offers higher magnetic moments, while the latter facilitates easier miniaturization and

Manuscript received: April, 29, 2024; Revised June, 27, 2024; Accepted June, 27, 2024.

This paper was recommended for publication by Editor-in-Chief Tamim Asfour and Editor Jessica Burgner-Kahrs upon evaluation of the Associate Editor and Reviewers' comments. This work was supported in part by the Engineering and Physical Sciences Research Council under Grants EP/R045291/1 and EP/V009818/1, and in part by the European Research Council under the European Union's Horizon 2020 Research and Innovation Programme under Grant 818045.

[1]Nikita Murasovs, Vittorio Francescon, Peter Lloyd, Michele Di Lecce, James H Chandler and Pietro Valdastri are with the Institute of Autonomous Systems and Sensing (IRASS), School of Electronic and Electrical Engineering, University of Leeds, Leeds, United Kingdom. Emails: [elnmur, el21vf, p.lloyd, elmdl, j.h.chandler, p.valdastri]@leeds.ac.uk

[2]Damith S Chathuranga is with the Department of Mechanical Engineering, University College London. Email: d.vithanage@ucl.ac.uk

[3]Giovanni Pittiglio is with Boston Children's Hospital, Harvard Medical School. Email: giovanni.pittiglio@childrens.harvard.edu

[4]Onaizah Onaizah is with the Department of Computing and Software, McMaster University. Email: onaizaho@mcmaster.ca

Digital Object Identifier (DOI): see top of this page.

maintains a fully soft approach.

MCRs which are 3 orders of magnitude softer than commercial counterparts [14] maneuver through complex anatomical structures by manipulating an external magnetic field to aid their movement. Previous studies have shown successful navigation of simulated human bronchial tree models [7, 8], the human pancreatic duct [15], and the neurovasculature [16]. Current research is delving into the possibilities of scaling down MCRs for medical procedures and navigation [17, 18, 19]. Yet, the influence of lung dynamics on magnetic robotic bronchoscopy has not been taken into account and remains a crucial area requiring further exploration.

The achievement of multipoint shape control of an MCR [6, 11, 8] is essential as it allows precise maneuvering with minimal contact, thus significantly reducing the risk of unintended injury and discomfort for the patient and improving targeting accuracy [7, 8]. Research has demonstrated the efficacy of this approach, resulting in a 50% improvement in tracking accuracy, a 50% reduction in contact time with obstacles during navigation compared to tip-only control, and a 90% decrease in targeting errors [7]. In [8], the MCR is deployed from a conventional bronchoscope, similar to the scenario envisaged in this paper. An illustrative overview of this process is given in Fig. 1.

Despite this progress, all proposed solutions for robotic bronchoscopy in the literature have thus far assumed the human lung anatomy to be static [7, 8]. This simplification disregards the dynamics of human respiration and the associated disturbance on any attempted anatomical navigation. Branches of the bronchial tree can move as much as 25 mm between the peaks of inspiration and exhalation [20, 21]. During bronchoscopy, patient breathing is controlled via a ventilation volume which assists in reducing pathway variations due to breathing but does not eliminate them [22]. Such a displacement would cause inadvertent contact between the robot and the tissue, resulting in unpredictable behavior. This is particularly prominent in bifurcations such as that shown in Fig. 2a, where unpredictable behaviors can cause the robot to navigate into an unplanned bronchial branch. This outlines the need for the development of a dynamic controller that would compensate for any disturbance associated with the human respiratory cycle. Natural breathing motion contributes to navigation inaccuracy due to the changing position of the target area and thus decreases the diagnostic yield [23], especially for tumors smaller than 20 mm. Researchers in [24] presented their solution for adjusting the catheter's navigation to respiratory motion; however, in their approach, the catheter's tip is adjusted in a stepwise fashion and remains static during a certain phase of the respiratory cycle. In our approach, the catheter's shape is adjusted synchronously to the respiratory cycle at all times.

In this work, we present a novel method for designing a soft magnetic catheter to be deployed from the instrument channel of a bronchoscope as in [8]. The design of the MCR incorporated the dynamic deformations of the bronchial tree such that it can compensate for the dynamic motion of the lungs by modulating its shape in a cyclical manner. To demonstrate this approach, we evaluated three different bronchial branches (up to 4th generation) and designed and manufactured separate MCRs specific to the breathing cycle motions of each branch. Furthermore, we employed a dynamic phantom to simulate the respiratory cycle of the bronchial tree, showing the influence of breathing on autonomous bronchial navigation, as well as presented the method to compensate for that. This will allow more accurate deep lung navigations and hence increase the diagnostic yield and lower the risk of inadvertent injury during bronchoscopy.

II. Methodology

In this section, we introduce the processes and methods used to design a MCR that can adapt its shape to the cyclically varying shape of the bronchial tree. The anatomical pathways actuation method, optimization principles, manufacturing steps and control strategy are considered.

A. Anatomical Data

To navigate the bronchial tree in a contact-minimized fashion, we optimize for the catheter's pose to be co-linear to the centerlines of the bronchial tree. To proceed to this optimization of the catheter's magnetic profile and design of the dynamic controller, it was necessary to first obtain the deformation of the bronchial centerlines and determine how rapidly those deformations occur.

A 4D-Lung dataset [25] provided by The Cancer Imaging Archive (TCIA) [26] was used to extract clinically relevant dynamic bronchial tree information. The 4D-Lung dataset is a collection consisting of images of 20 locally-advanced, non-small cell lung cancer patients; including four-dimensional (4D) computed tomography (CT) data, acquired with fan beam CT (4D-FBCT) and 4D cone beam CT (4D-CBCT), providing spatial as well as temporal data [25]. Data from Subject ID - 100_HM10395 were used for the purposes of this study, as it presents the highest resolution with pixel size of 0.9766 mm and CT slice distance of 3 mm. The data contain chest CT images of the patient during the full respiratory cycle which is split into 10 breathing phases. The cycle starts at the peak exhalation (PE) or 0%, then reaches the peak inhalation (PI) around 50%, before returning toward PE such that 100% = 0%.

CT images for each of the 10 time steps were separately segmented using 3D Slicer software with the Airway Segmentation module [27]. Segmented tissues were then reconstructed to produce 3D models of the bronchial tree. Subsequently, the Vascular Modeling Toolkit was used to extract centerlines of the bronchial tree up to 4th generation of branches at each time step. The extracted centerlines at PE (0%) are overlaid on the original CT image in Fig. 2a. Three bronchial branches (see Fig. 2a) were selected to serve as a test case for this work. The diameters of the lumens at the end of Branch 1, Branch 2 and Branch 3 are 4.5 mm, 4.6 mm, 3.8 mm respectively.

B. Designing & Optimizing the Magnetic Profile of MCR

In the proposed approach, a standard bronchoscope is used to enter and navigate through the trachea. Afterwards, the

This article has been accepted for publication in IEEE Robotics and Automation Letters. This is the author's version which has not been fully edited and content may change prior to final publication. Citation information: DOI 10.1109/LRA.2024.3426385

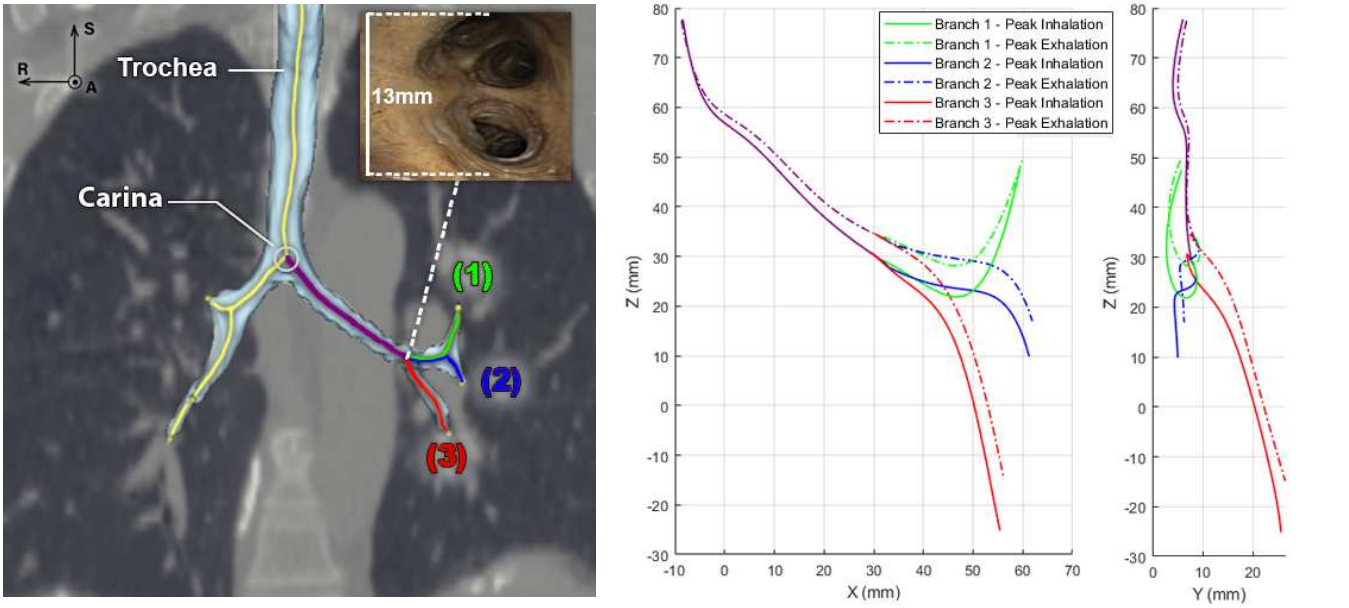

(a) (b)

Fig. 2. (a) CT data of the patient's lungs [25] at the start of the respiratory cycle with light blue volume showing the result of bronchial tree segmentation and yellow lines outlining computed centerlines of the airways; three branches that were selected for experiments are identified with number 1-3 and highlighted in green, blue and red respectively. Arrows represent the orientation of the CT slice, where R - right, A - anterior, and S - superior. The bronchial tree was segmented up to 4th generation of branches. Example of a bronchial bifurcation viewed from a bronchoscope camera is also shown (from [8]). (b) Three dimensional dynamic deformations that occur during the entire respiratory cycle (frontal plane on the left and sagittal plane on the right) with Branch 1 in green, Branch 2 in blue, and Branch 3 in red. Peak inhalations (PI) are shown as solid lines, and peak exhalations (PE) are shown as dashed dotted lines.

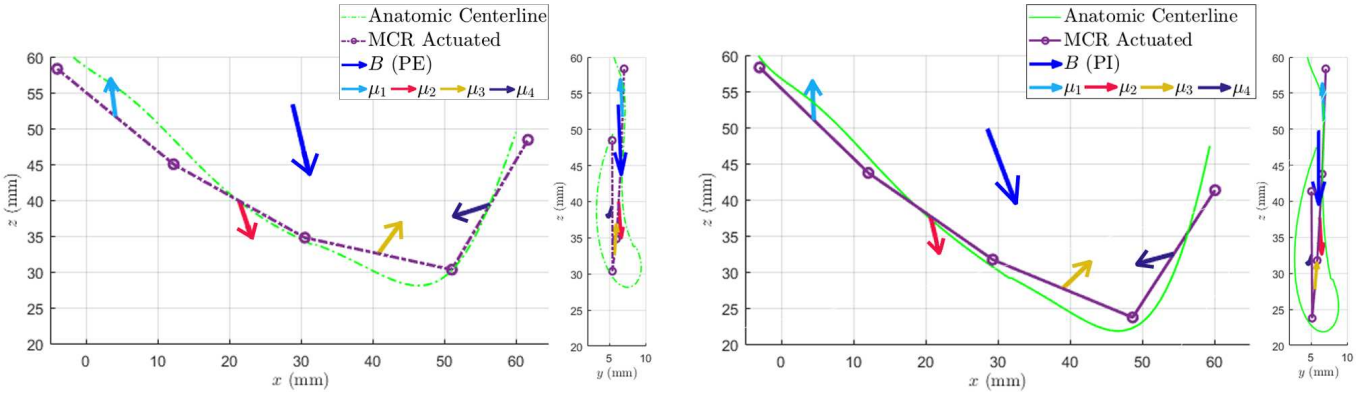

(a) Peak Exhalation (b) Peak Inhalation

Fig. 3. Result of the optimization algorithm (sample Branch 1) for peak exhalation (PE) and peak inhalation (PI), with the anatomic centerline of the bronchial tree in green lines, and rigid-link model actuated by external magnetic field (B) in purple lines. The magnetic field direction in the global reference frame is shown as a blue arrow, and is different for PE and PI. The directions of magnetizations for each link (μ_i) relative to link orientations are also given.

MCR is deployed from the instrument channel of the bronchoscope to navigate the bronchial tree to the region of interest (see Fig. 1). The total length of MCR was set to match the length of the branch (from the carina to the 4th generation of branches), which is around 80 mm.

A rigid-link model was implemented to design a magnetic profile for MCR and the corresponding magnetic fields that would allow accurate shape formation that can adapt to the deformation of the bronchial tree. Using a higher number of sections leads to higher dexterity but comes at the expense of more complex and cumbersome optimization and control [6, 8]. For this application, 4 sections of 20 mm in length were found to provide a sufficient balance for the desired task.

Using the anatomical deformations of the bronchial tree at PE and PI, we parametrize the angles (i.e. $\boldsymbol{Q_{PE}}$ and $\boldsymbol{Q_{PI}}$ respectively) of our rigid-link model to conform to the desired shapes (see Fig. 3). By optimizing the magnetic profile of the MCR to conform its shape to the centerline of the bronchial tree throughout the whole navigation (including dynamic changes of the centerline due to respiration), the MCR will have minimal contact with the environment; hence the influence of the lumen interactions can be omitted from the model.

The process of optimizing the magnetic profile of the MCR consists of finding the magnetization ($\boldsymbol{\mu_i}$) of each section (L_i) (i.e. each rigid-link) which, in combination with the global

homogeneous applied magnetic field ($\boldsymbol{B}$) will deform the MCR to the predetermined desired shape (see Fig. 3) [6]. This optimization process is based on balancing elastic, magnetic and gravitational forces, and torques (wrenches) acting on the MCR during actuation. The elastic torques can be derived as:

$$\mathbf{T_e}^{(3\times k)} = \boldsymbol{K}^{(3\times 3)}\, \boldsymbol{Q}^{(3\times k)} \tag{1}$$

where k is the number of rigid links inserted at a given time, Q is a matrix of joint angles (3 degrees of freedom for each link), $\mathbf{T_e}$ is the resulting elastic torque matrix [28], and K is the diagonal stiffness matrix defined by the bending and torsional products of Young's Modulus (E) and second moment of intertia (I). This assumption of linear joint stiffness is valid when the length of each link is sufficiently small [29].

Assuming homogeneous magnetic field, magnetic torques are defined as:

$$\mathbf{T_m}^{(3\times k)} = \boldsymbol{J}^{(3\times 3k)^T}\, (\hat{\boldsymbol{S}}^{(3k\times 3)}\, \boldsymbol{B}^{(3\times k)}) \tag{2}$$

where $\boldsymbol{J}^T$ is the Jacobian transpose of the MCR, $\boldsymbol{B}$ is the magnetic field, $\hat{\boldsymbol{S}}$ is the skew matrix of magnetizations defined as:

$$\hat{\boldsymbol{S}}^{(3k\times 3)} = \begin{bmatrix} -\boldsymbol{\mu_k}_\times \\ -\boldsymbol{\mu_{k-1}}_\times \\ \vdots \\ -\boldsymbol{\mu_1}_\times \end{bmatrix} \quad \text{since} \quad \boldsymbol{B}\times\boldsymbol{\mu_i} = -\boldsymbol{\mu_i}_\times \boldsymbol{B} \tag{3}$$

where $(.)_\times$ is the skew operator.

$\boldsymbol{G}$ is the gravitational component defined as:

$$\boldsymbol{G}^{(3k\times k)} = -\begin{bmatrix} \boldsymbol{e_3}^{(3)} \\ \boldsymbol{e_3}^{(3)} \\ \vdots \\ \boldsymbol{e_3}^{(3)} \end{bmatrix} \begin{bmatrix} m_1 & m_2 & \cdots & m_k \end{bmatrix} \tag{4}$$

where m is the mass of each link.

In an equilibrium configuration, mechanical, gravitational and magnetic torques sum to zero. Hence, the magnetic profile of the MCR can be optimized subject to:

$$min_{\mu,B_{PE}} \mid K\, Q_{PE} - J^T\, (S\, B + G) \mid \tag{5}$$

for PE, and

$$min_{\mu,B_{PI}} \mid K\, Q_{PI} - J^T\, (S\, B + G) \mid \tag{6}$$

for PI.

Hence, to optimize the magnetic profile of the MCR such that it conforms its shape to the centerline of bronchial tree throughout the whole navigation (insertion and dynamic influence due to breathing) the (5) and (6) should be satisfied for all steps of insertion (i.e. $k = 1, 2, 3, 4$) and for multiple joint angle configurations (i.e. $\boldsymbol{Q_{PE}}$ and $\boldsymbol{Q_{PI}}$) simultaneously. An example result of the optimization process can be seen in Fig. 3, where the magnetization directions for each link and the direction of the applied magnetic field are shown, giving the resultant configuration of MCR at PE and PI. The magnetic profile stays the same (due to the nature of magnetically hard matter) while shape compensation is reached by adjusting the external magnetic field ($\boldsymbol{B}$). The result of this optimization method is a predefined magnetic profile (i.e. magnetization of each link - $\boldsymbol{\mu_i}$), and the corresponding external magnetic field ($\boldsymbol{B}$), specific to the current insertion step and the stage of the breathing cycle. Navigation using this model is performed quasi-statically.

C. Experimental setup

A Tri-axial Helmholtz coil platform (3DXHC12.5-300, Dexing MagnetTech. Co., Ltd, Xiamen, China) was used for the generation of homogeneous magnetic fields. The platform uses 3 power supply units (PSU) (DXKDP, Dexing Magnet Tech. Co., Ltd, Xiamen, China) to generate current in the coils and can establish any 3-dimensional magnetic field up to 25 mT at 0.5 Hz. This method allows us to accurately and repeateably influence the applied external field and thus the shape of MCR continuously.

The MCR was fixed in the workspace at a predefined initial rotation, mimicking the deployment angle from a bronchoscope [6, 8]. It was quasi-statically actuated using magnetic fields calculated from (5) and (6) and inserted via a stepper motor (as in [7]). The deformation was captured using a Basler camera (acA2040-120uc Basler AG, Ahrensburg, Germany) with a Basler C23-3518-5M-P f35 mm lens, against a white background to enhance contrast for image segmentation and results parameterization. The mapping between physical dimensions and the pixels of the image was done using the known diameter of the MCR (2 mm). This was further improved by calibrating the camera, where we placed the camera in a fixed location (that used for the actual experiments), inserted the tentacle to hang in the workspace adjacent to a checkerboard pattern. We used Matlab's Camera Calibration package to remove lens distortion effects from the image. This facilitated the acquisition of the MCR deformations within a two-dimensional (2D) framework, a practice deemed acceptable due to the relatively shallow depth of field, proportionate to the deformations occurring within the plane. The majority of bronchial deformations (95%) happen within the plane, while the out-of-plane geometry can be navigated by adjusting the initial orientation of the tip of the bronchoscope. The outline of the experimental setup is given in Fig. 4.

To simulate the dynamic nature of the bronchial tree, the design of the phantom for this experiment consisted of 4 linear actuators (L12-30-50-6-R, Actuonix, Canada) which have a maximum speed of 25 mm/s. The phantom is constructed from plastic rings attached to the linear actuators, simulating the lumen cross-sections. These are horizontally positioned on the interface to mimic out-of-plane deformations in accordance to the anatomic model in Fig. 2b and move the lumen cross-sections synchronously with the anatomic displacements of the bronchial tree. Linear actuators iterate over all 10 breathing phases (see Sec. II-A) every 0.8 second, completing the entire breathing cycle in 8 seconds. The MCR is autonomously inserted by 10 mm at PE (i.e. every 8s) into the workspace through an insertion tube by a stepper motor. This process is repeated until the end of autonomous navigation. See Fig. 5 for the full overview of the dynamic phantom.

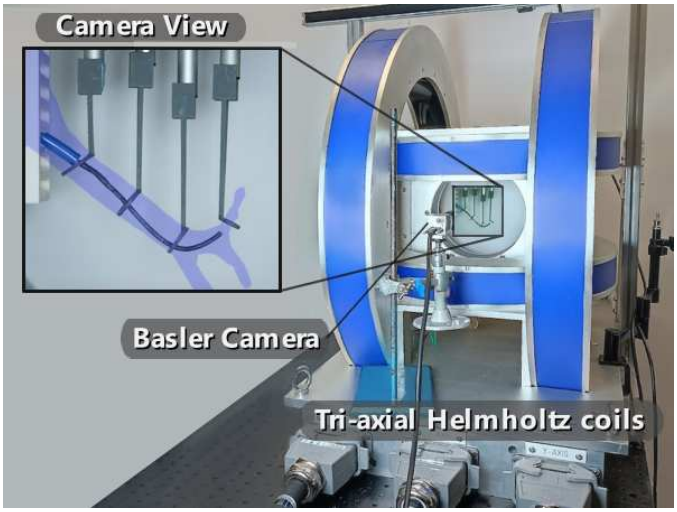

Fig. 4. Experimental setup overview with Tri-axial Helmholtz coils for the actuation of the MCR. Basler camera is used to capture the image of the scene in high resolution. The MCR is being autonomously inserted into the workspace through a rigid tube that simulates deployment from a bronchoscope. The rigid tube has a predefined orientation obtained from the optimization algorithm. Bronchial tree is overlaid on top of the camera view for reference.

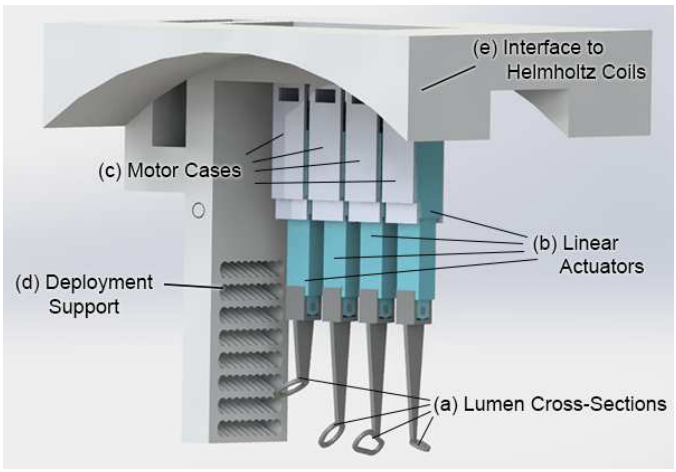

Fig. 5. Overview of the dynamic phantom. (a) Lumen cross-sections made out of plastic rings. (b) Linear actuators used to dynamically move the plastic rings in accordance to the actual bronchial tree displacements. (c) 3D printed plastic cases for the motors to adjust horizontal positioning (see Fig. 2b) and attach each motor to the interface. (d) Punctured wall to provide the initial orientation to the insertion tube. (e) Mounting interface which is set on Helmholtz coils and provides horizontal alignment.

The average respiratory cycle of an adult patient is between 3 to 5 seconds [30]. Due to hardware specific limitations of the actuating frequency of our Helmholtz coils, the period of the respiratory cycle used in this study is longer than that however, the same approach can be readily applied to a faster field generation setup [31] without any major modifications, and the same results would apply.

D. Manufacturing of MCR

High magnetic fields necessary for optimal deformation often lead to instability, resulting in unpredictable deformations [32]. To address this, we modified the MCR fabrication process based on [15], significantly enhancing torsional stiffness (by 100 times) while increasing the linear stiffness by only 5 times using a braided structure. This addition effectively reduces magnetic instability while maintaining the overall design generally soft in bending.

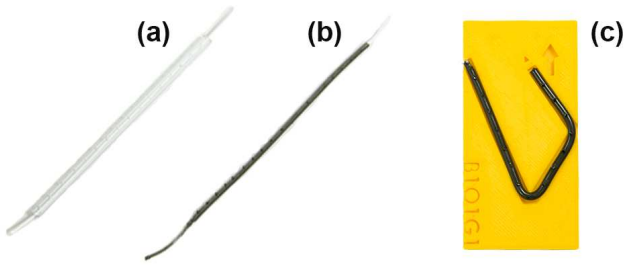

Fig. 6. Manufacturing process of MCR. (a) Braid threaded through a custom 2 mm internal diameter perspex tube (b) MCR with braided reinforcement and defined protuberances removed from tube after curing (c) MCR placed in a bespoke magnetizing tray to be magnetized to saturation under a large uniform field B.

The manufacturing process, depicted in Fig. 6, involves laser cutting a perspex tube, drilling 0.5 mm holes at 5 mm intervals for visual reference during deformation. Subsequently, silicone (Ecoflex-0030, Smooth-On Inc., USA) is mixed with neodymium-iron-boron microparticles with an average diameter of 5 μm (MQFP-B+, Magnequench GmbH, Germany) in a 1:1 mass ratio to create soft magnetic matter. A nylon braid (Everlasto - James Lever 1856 Ltd., Manchester, U.K.) of external diameter 1 mm is aligned within the tube before filling with the silicone mixture. After curing at room temperature for four hours, the MCR is removed, trimmed, and placed in a magnetization tray (see Fig. 6c) to be magnetized under a 4.66 T saturating field (ASCIM-10-30, ASC Scientific, USA). [6, 8].

The process yields longitudinally braid-reinforced MCRs, 80 mm long and 2 mm in diameter, optimized for the breathing cycle's full motion. For more details, see [15] and Fig. 6(a-b).

III. Results

In these experiments, we assumed the generated magnetic field to be uniform across the entire workspace. Furthermore, using a rigid-link model implies the assumption that all deformations of silicone are elastic, and do not present any non-linear behaviour and hysteresis.

A. Autonomous Navigation

This test evaluated the accuracy of autonomous navigation of MCRs through a bronchial phantom that dynamically simulates respiratory displacements. The test compared performances with and without compensation.

Figure 7 illustrates the MCR's navigation through the bronchial tree. Each branch (1-3) was navigated using an MCR with a magnetic profile specifically optimized for that branch. The uncompensated navigation used a model based on a single deformation at peak exhalation, while the compensated navigation used deformations across the entire breathing cycle (see Sec. II-B for optimization details).

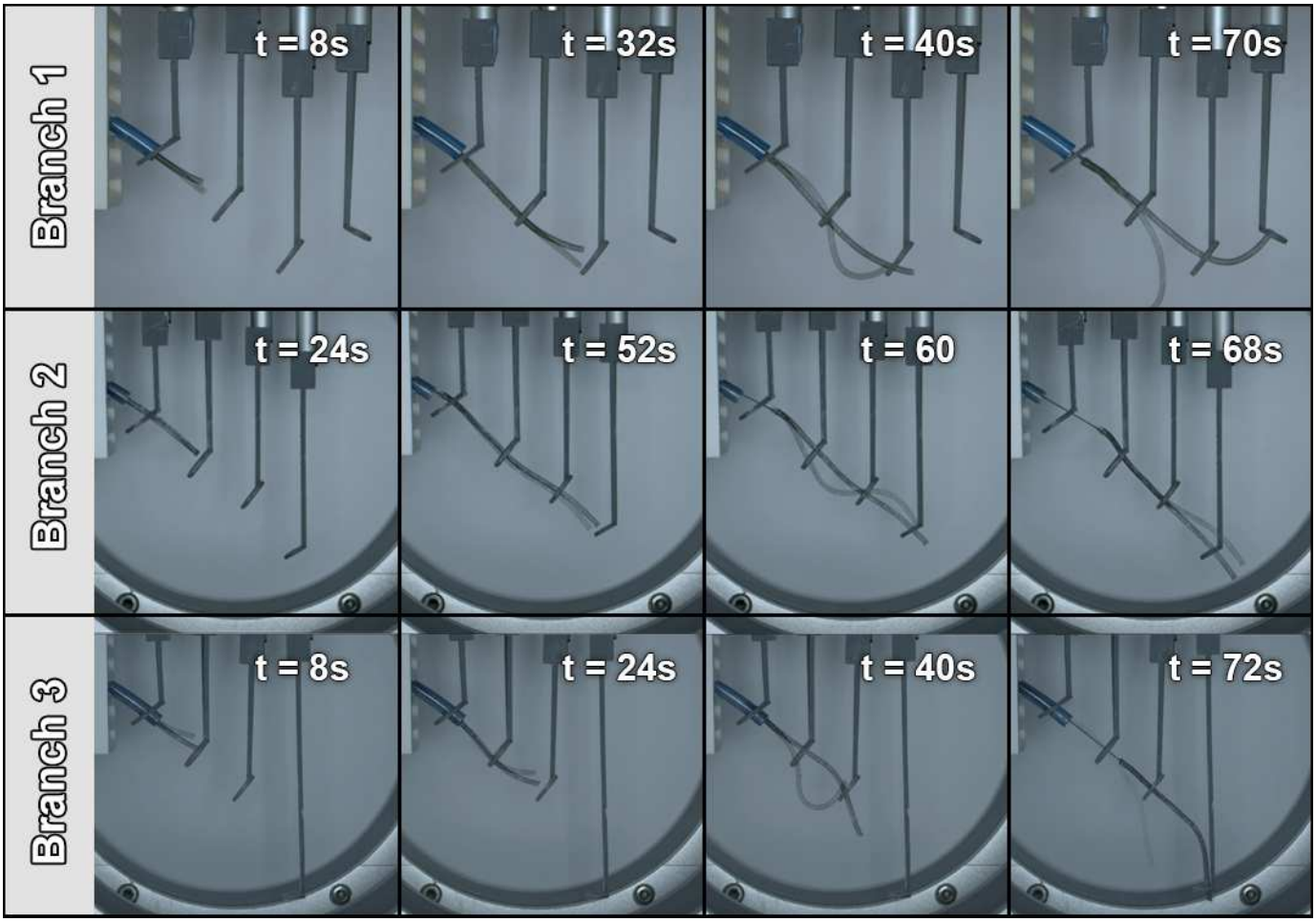

Fig. 7. Time series showing the MCR's navigation through the dynamically-acutated bronchial branches (1-3). Three different MCRs are used in total, where each has a unique magnetic profile optimized for the shape of that particular bronchial branch. Both the results of navigation with and without compensation are presented, where the results of no compensation are overlaid with lower opacity. The autonomous navigation of the MCR with compensation is capable of dynamically adjusting its shape to the bronchial centerline, which allows navigation through all the plastic rings.

The experiments were conducted three times, and the results reported are RMS averages. Examples from these navigations can be viewed in Supplementary Video 1.

B. Error Metrics

For this work, we have used two metrics commonly used in other similar works [33, 7] to define the error in the conformation of MCR to the centerline of the bronchial tree: Root Mean Square (RMS) and weighted Root Mean Square (wRMS). We present the average error for each branch computed across all time phases.

Root Mean Square error is a metric of the overall accuracy of shape-forming of MCR compared to the CT branch centerline. It was computed using the following formula:

$$e_{rms} = \sum_{t=1}^{T} \sqrt{\frac{1}{N} \sum_{i=1}^{N} d_i^2} \tag{7}$$

where N is the total number of data points confining MCR shape, and d_i is the distance of each of these points to its closest counterpart on the CT data centerline.

To analyse how accurately the tip of the MCR matches the distal location of the bronchial branch we use the wRMS as:

$$e_{wrms} = \sum_{t=1}^{T} \sqrt{\frac{1}{N} \sum_{i=1}^{N} (d_i^2 \, \hat{s}_i)} \tag{8}$$

where all variables are the same as introduced above but d is multiplied on $\hat{s}$ which is the normalized distance along the MCR with the proximal end being $\hat{s} = 0$ and the distal end being $\hat{s} = 1$. The idea of this metric is to penalize MCR more for deviations around the branch bifurcations (distal end of the branch) as they have more influence over successful navigation. The RMS and wRMS data were subsequently refined through the application of a Savitzky-Golay filtering process.

Figure 8 shows an example of how RMS and wRMS values vary throughtout the navigation of the MCR in Branch 1 with compensation. The navigation without compensation is not shown due to failure occuring at $t = 40s$ (see Fig. 7). Table I provides these error metrics for the navigations into all three branches, with and without compensation.

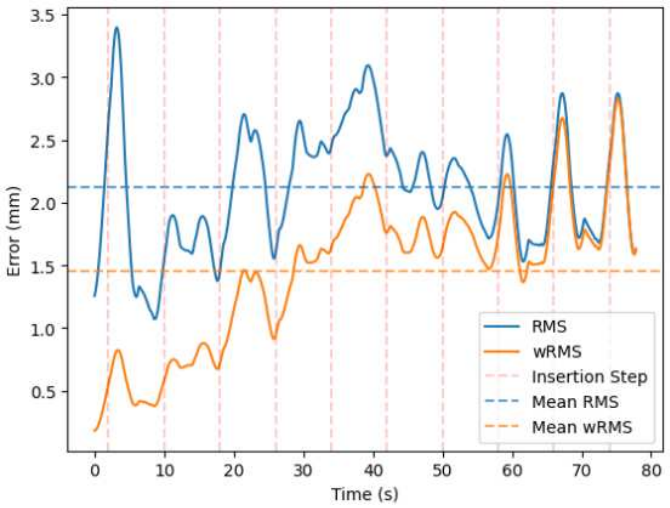

Fig. 8. Plot of the RMS and wRMS errors over time for autonomous navigation of Branch 1 with compensation. Blue solid line for RMS values, and orange solid line for wRMS values. Mean values are given as dashed horizontal lines. The timestamps at which the insertion happens are plotted as vertical red lines.

TABLE I. Average Root Mean Square and Average Weighted Root Mean Square for all branches across the entire navigation. Both, with and without compensation, error metrics are given.

Branch ID		Mean RMS (mm)	Mean wRMS (mm)
Branch 1	With Comp.	2.1	1.3
	Without Comp.	-	-
Branch 2	With Comp.	1.4	0.9
	Without Comp.	4.3	4.6
Branch 3	With Comp.	1.9	1.2
	Without Comp.	-	-

IV. Discussion

The bronchial tree, with its multiple bifurcations affected by respiratory dynamics, poses challenges for autonomous bronchial navigation, risking adverse outcomes (see Fig. 2a). Dynamically adapting the shape of the MCR to the bronchial tree's centerline is essential to counter these displacements caused by respiration.

Despite slower respiration rates in this study compared to real-life conditions, the MCR's settling time of approximately 0.35 seconds is significantly faster than the actuation step of 0.8 seconds (see supplementary Video 1). This suggests the potential for real-life application, especially since clinical settings often involve controlled respiration rates.

In Fig. 7, the experiment shows that navigations of MCR into all three branches that did not consider bronchial dynamics (i.e. without compensation) resulated into failure, either partial like missing a plastic lumen in Branch 2 or complete as in Branches 1 and 3. Furthermore, navigations without compensation do not follow the centerline of the bronchial tree and result in a wrong orientation before entering the next plastic ring, as in Branch 1 ($t = 32s$), in Branch 2 ($t = 52s$), and in Branch 3 ($t = 24s$) in Fig. 7. The system is not aware of such complication, and continues to insert the MCR autonomously, resulting in a further deterioration of the problem as can be seen in Branch 1 ($t = 40s$), in Branch 2 ($t = 60s$), and in Branch 3 ($t = 40s$) in Fig. 7. In Branches 1 and 3, the MCR was not able to correct its shape which caused a critical instability followed by a navigation failure. In the case of Branch 2, the MCR managed to correct its shape through interaction with the environment but then failed to navigate through the last plastic ring. This is a characteristic of this experiment but in a clinical scenario the dynamic displacements of bifurcations such as that demonstrated would cause undesired interaction with the anatomy and potential "wrong turns" during autonomous navigation.

The RMS and wRMS plots (see Fig. 8) show the majority of spikes in shape errors occur after the insertion step. Afterwards, the MCR is able to correct its shape by conforming to the centerline. The values of wRMS converge to the values of RMS at the end of the navigation, pointing out that the majority of the shape error occurs at the distal end of the MCR. Despite that, the values of both RMS and wRMS remain lower than the associated bronchial diameters (presented in Sec. II-A) throughout the entire navigation.

Table I reveals a significant reduction in navigation errors for Branch 2, while Branches 1 and 3 experienced navigation failures when un-adapted.

V. Conclusion

This paper presented an analysis of the respiratory cycle's impact on MCR navigation and provided a method for compensating for such influence. Starting with CT data segmentation, we have parameterized geometrical changes in the bronchial tree structure that occur during respiration. We then gave a design outline of how one can manufacture a MCR with a magnetic profile optimized for deformations at both the PE and at the PI, resulting in the ability to dynamically compensate for such anatomical deformations. We showed how using magnetizations and magnetic fields derived from the mechanical-magnetic equilibrium equation, MCRs can shape-form to track the curvature of the bronchial tree and dynamically realign with the centerline of the bronchial branches. In our experiments, we have shown how the influence of human respiration will affect an autonomous navigation and provided a method to compensate for such dynamics. Overall, three diverse bronchial branches were used in this work, which showed the error in shape-forming (RMS value) of 2.1 mm, 1.4 mm and 1.9 mm, and the error in tip-positioning (wRMS value) of 1.3 mm, 0.9 mm and 1.2 mm. In the cases of Branch 1 and 3, compensating for bronchial dynamics resulted in avoidance of failed navigation, whereas in the case of Branch 2, compensated navigation provided a substantially lower error.

Our experiment showed the possibility of this method to adapt the shape of MCR to the anatomic deformations of the bronchial tree during navigation. Despite that, additional work has to be done in this area to improve the overall accuracy of shape-forming (especially for more tortuous pathways such as Branch 1 and Branch 3) as well as higher frequency actuation to be able to perform real-time experiments and the ability of compensate in a closed-loop fashion. Furthermore, in future work we aim to examine the feasability of this method on a broader range of anatomies.

REFERENCES

[1] J. Puchalski, "Robotic bronchoscopy for the diagnosis of peripheral lung nodules: a review," *Current Pulmonology Reports*, vol. 10, no. 1, pp. 46–52, 2021.

[2] A. C. Chen, N. J. Pastis, M. S. Machuzak, T. R. Gildea, M. J. Simoff, C. T. Gillespie, A. K. Mahajan, S. S. Oh, and G. A. Silvestri, "Accuracy of a robotic endoscopic system in cadaver models with simulated tumor targets: Access study," *Respiration*, vol. 99, no. 1, pp. 56–61, 2020.

[3] T. da Veiga, J. H. Chandler, P. Lloyd, G. Pittiglio, N. J. Wilkinson, A. K. Hoshiar, R. A. Harris, and P. Valdastri, "Challenges of continuum robots in clinical context: a review," *Progress in Biomedical Engineering*, vol. 2, no. 3, p. 032003, 2020.

[4] M. McCandless, A. Perry, N. DiFilippo, A. Carroll, E. Billatos, and S. Russo, "A soft robot for peripheral lung cancer diagnosis and therapy," *Soft Robotics*, vol. 9, no. 4, pp. 754–766, 2022.

[5] Y. Li, J. Peine, M. Mencattelli, J. Wang, J. Ha, and P. E. Dupont, "A soft robotic balloon endoscope for airway procedures," *Soft Robotics*, vol. 9, no. 5, pp. 1014–1029, 2022.

[6] G. Pittiglio, A. L. Orekhov, T. da Veiga, S. Calò, J. H. Chandler, N. Simaan, and P. Valdastri, "Closed loop static control of multi-magnet soft continuum robots," *IEEE Robotics and Automation Letters*, 2023.

[7] G. Pittiglio, P. Lloyd, T. da Veiga, O. Onaizah, C. Pompili, J. H. Chandler, and P. Valdastri, "Patient-specific magnetic catheters for atraumatic autonomous endoscopy," *Soft Robotics*, vol. 9, no. 6, pp. 1120–1133, 2022.

[8] G. Pittiglio, J. H. Chandler, T. da Veiga, Z. Koszowska, M. Brockdorff, P. Lloyd, K. L. Barry, R. A. Harris, J. McLaughlan, C. Pompili, and P. Valdastri, "Personalized magnetic tentacles for targeted photothermal cancer therapy in peripheral lungs," *Communications Engineering*, vol. 2, no. 1, p. 50, Jul 2023. [Online]. Available: https://doi.org/10.1038/s44172-023-00098-9

[9] J. Edelmann, A. J. Petruska, and B. J. Nelson, "Magnetic control of continuum devices," *The International Journal of Robotics Research*, vol. 36, no. 1, pp. 68–85, 2017.

[10] S. Yim, E. Gultepe, D. H. Gracias, and M. Sitti, "Biopsy using a magnetic capsule endoscope carrying, releasing, and retrieving untethered microgrippers," *IEEE Transactions on Biomedical Engineering*, vol. 61, no. 2, pp. 513–521, 2013.

[11] M. Richter, V. K. Venkiteswaran, and S. Misra, "Multi-point orientation control of discretely-magnetized continuum manipulators," *IEEE Robotics and automation letters*, vol. 6, no. 2, pp. 3607–3614, 2021.

[12] Y. Kim, G. A. Parada, S. Liu, and X. Zhao, "Ferromagnetic soft continuum robots," *Science Robotics*, vol. 4, no. 33, p. eaax7329, 2019.

[13] G. Z. Lum, Z. Ye, X. Dong, H. Marvi, O. Erin, W. Hu, and M. Sitti, "Shape-programmable magnetic soft matter," *Proceedings of the National Academy of Sciences*, vol. 113, no. 41, pp. E6007–E6015, 2016.

[14] L. Blanc, A. Delchambre, and P. Lambert, "Flexible medical devices: Review of controllable stiffness solutions," in *Actuators*, vol. 6, no. 3. MDPI, 2017, p. 23.

[15] P. Lloyd, O. Onaizah, G. Pittiglio, D. K. Vithanage, J. H. Chandler, and P. Valdastri, "Magnetic soft continuum robots with braided reinforcement," *IEEE Robotics and Automation Letters*, vol. 7, no. 4, pp. 9770–9777, 2022.

[16] Y. Kim, E. Genevriere, P. Harker, J. Choe, M. Balicki, R. W. Regenhardt, J. E. Vranic, A. A. Dmytriw, A. B. Patel, and X. Zhao, "Telerobotic neurovascular interventions with magnetic manipulation," *Science Robotics*, vol. 7, no. 65, p. eabg9907, 2022.

[17] L. Hines, K. Petersen, G. Z. Lum, and M. Sitti, "Soft actuators for small-scale robotics," *Advanced materials*, vol. 29, no. 13, p. 1603483, 2017.

[18] Y. Kim, H. Yuk, R. Zhao, S. A. Chester, and X. Zhao, "Printing ferromagnetic domains for untethered fast-transforming soft materials," *Nature*, vol. 558, no. 7709, pp. 274–279, 2018.

[19] J. A. Carpenter, T. B. Eberle, S. Schuerle, A. Rafsanjani, and A. R. Studart, "Facile manufacturing route for magneto-responsive soft actuators," *Advanced Intelligent Systems*, vol. 3, no. 8, p. 2000283, 2021.

[20] S. Miyawaki, S. Choi, E. A. Hoffman, and C.-L. Lin, "A 4dct imaging-based breathing lung model with relative hysteresis," *Journal of computational physics*, vol. 326, pp. 76–90, 2016.

[21] V. Boldea, G. C. Sharp, S. B. Jiang, and D. Sarrut, "4d-ct lung motion estimation with deformable registration: quantification of motion nonlinearity and hysteresis," *Medical physics*, vol. 35, no. 3, pp. 1008–1018, 2008.

[22] D. Georgopoulos and C. Roussos, "Control of breathing in mechanically ventilated patients," *European Respiratory Journal*, vol. 9, no. 10, pp. 2151–2160, 1996.

[23] D. Van Lewen, T. Janke, H. Lee, R. Austin, E. Billatos, and S. Russo, "A millimeter-scale soft robot for tissue biopsy procedures," *Advanced Intelligent Systems*, p. 2200326, 2023.

[24] A. Kuntz, M. Emerson, T. E. Ertop, I. Fried, M. Fu, J. Hoelscher, M. Rox, J. Akulian, E. A. Gillaspie, Y. Z. Lee *et al.*, "Autonomous medical needle steering in vivo," *Science Robotics*, vol. 8, no. 82, p. eadf7614, 2023.

[25] G. D. Hugo, E. Weiss, W. C. Sleeman, S. Balik, P. J. Keall, J. Lu, and J. F. Williamson, "A longitudinal four-dimensional computed tomography and cone beam computed tomography dataset for image-guided radiation therapy research in lung cancer," *Medical physics*, vol. 44, no. 2, pp. 762–771, 2017.

[26] K. Clark, B. Vendt, K. Smith, J. Freymann, J. Kirby, P. Koppel, S. Moore, S. Phillips, D. Maffitt, M. Pringle *et al.*, "The cancer imaging archive (tcia): maintaining and operating a public information repository," *Journal of digital imaging*, vol. 26, no. 6, pp. 1045–1057, 2013.

[27] P. Nardelli, K. A. Khan, A. Corvò, N. Moore, M. J. Murphy, M. Twomey, O. J. O'Connor, M. P. Kennedy, R. S. J. Estépar, M. M. Maher *et al.*, "Optimizing parameters of an open-source airway segmentation algorithm using different ct images," *Biomedical engineering online*, vol. 14, no. 1, pp. 1–24, 2015.

[28] V. K. Venkiteswaran, J. Sikorski, and S. Misra, "Shape and contact force estimation of continuum manipulators using pseudo rigid body models," *Mechanism and machine theory*, vol. 139, pp. 34–45, 2019.

[29] D. C. Rucker and R. J. Webster III, "Statics and dynamics of continuum robots with general tendon routing and external loading," *IEEE Transactions on Robotics*, vol. 27, no. 6, pp. 1033–1044, 2011.

[30] G. Yuan, N. A. Drost, and R. A. McIvor, "Respiratory rate and breathing pattern," *McMaster Univ. Med. J*, vol. 10, no. 1, pp. 23–25, 2013.

[31] R. Dreyfus, Q. Boehler, S. Lyttle, P. Gruber, J. Lussi, C. Chautems, S. Gervasoni, J. Berberat, D. Seibold, N. Ochsenbein-Kölble *et al.*, "Dexterous helical magnetic robot for improved endovascular access," *Science Robotics*, vol. 9, no. 87, p. eadh0298, 2024.

[32] P. Lloyd, Z. Koszowska, M. Di Lecce, O. Onaizah, J. H. Chandler, and P. Valdastri, "Feasibility of fiber reinforcement within magnetically actuated soft continuum robots," *Frontiers in Robotics and AI*, p. 214, 2021.

[33] P. Lloyd, G. Pittiglio, J. H. Chandler, and P. Valdastri, "Optimal design of soft continuum magnetic robots under follow-the-leader shape forming actuation," in *2020 International Symposium on Medical Robotics (ISMR)*. IEEE, 2020, pp. 111–117.